



CrossMark
click for updates

Cite this: *RSC Adv.*, 2016, 6, 59961

Hybrid polymer matrix composite containing polyaniline and Nafion as novel precursor of the enhanced catalyst for oxygen reduction reaction†

Xudong Fu,^{ab} Suli Wang,^a Huanqiao Li,^a Zhangxun Xia,^a Luhua Jiang^a and Gongquan Sun^{*a}

A hybrid polymer matrix composite has been synthesized by *in situ* polymerization of aniline monomers into Nafion framework and characterized by X-ray diffraction and thermo-gravimetric analysis, which serves as a novel nitrogen precursor for metal–nitrogen-doped carbon catalyst. The electrostatic interaction between the amino groups of polyaniline and sulfonate groups of Nafion is found to be helpful for the promotion of thermal stability of the nitrogen precursor, which increases the nitrogen content of the catalyst. High specific surface area can be achieved *via* the decomposition and volatilization of Nafion in the pyrolysis procedure. The half-wave potential of the Nfn/PA/Fe-2 catalyst is 0.879 V, larger than that of the commercial Pt/C catalyst ($E_{1/2} = 0.860$ V). After 5000 cycles in alkaline media, the half-wave potential of Nfn/PA/Fe-2 decreases by 19 mV, which exhibits the excellent electrochemical durability and promising application in fields of metal–air batteries and alkaline fuel cells.

Received 4th April 2016

Accepted 8th June 2016

DOI: 10.1039/c6ra08654c

www.rsc.org/advances

Introduction

Platinum (Pt) and Pt-based materials are considered to be the premium catalysts for the oxygen reduction reaction (ORR), which is one of the key reactions for renewable energy technologies (*i.e.*, fuel cells and metal–air batteries).¹ Because of the scarcity of Pt, the on-going search for Pt-free ORR catalysts has attracted much attention.^{2–4} Recent investigations have shown that metal–nitrogen-doped carbon (MNC) catalysts exhibit high activity as compared to Pt-based materials.^{5–8} However, the intrinsic ORR catalytic activity of a single active site in MNC catalyst is lower than for Pt-based catalyst.⁹ Catalytic activity of MNC material is proposed to be enhanced *via* the increase of the density of active site and/or specific surface area.¹⁰

The nitrogen-containing groups coordinated with metal ions have been demonstrated to be catalytically active for the ORR.^{11–13} It has also been reported that the nitrogen functionalities on the carbon surface are shown to be responsible for ORR activity, whereas the transition metals merely influence the other properties of the catalyst, such as electronic conductivity, morphology and nitrogen-doping level.^{14–16} It is challenging to prepare the catalyst with high nitrogen content, in that the nitrogen-containing precursors are readily to decompose and

volatilize during the heat treatment processes.^{17,18} Recently, significant progresses (*i.e.*, the use of nitrogen-containing precursors with high thermal stability, high pressure pyrolysis and “shape fixing *via* salt recrystallization”) have been achieved to increase the nitrogen content in the final catalysts.^{19–21} High specific surface area with a meso/micro multimodal pore size distribution could improve the ORR activity of MNC catalysts.²² It has been shown that rich microporosity can afford numerous active sites,²³ and high mesoporosity can promote the transport properties of O₂.²⁴ To obtain MNC catalysts with high porosity, different kinds of templates are often employed in the synthesis process.^{24,25} The highly active catalysts with high nitrogen content and large specific surface area have been obtained *via* two steps (hard-template synthesis of mesoporous carbon-based materials and then NH₃ activation to optimize both the porous structures and the surface nitrogen functionalities of the catalysts).²⁶ To the best of our knowledge, it is difficult to obtain MNC catalysts with high nitrogen content and large specific surface area in the absence of templates.

In this work, we report a template-free approach for the preparation of MNC catalyst with high nitrogen content and large specific surface area, which is achieved by pyrolysis hybrid polymer matrix composite and ferric chloride. A novel precursor of the hybrid polymer matrix composite has been synthesized by *in situ* polymerization of aniline monomers into Nafion framework and characterized by X-ray diffraction and thermo-gravimetric analysis. The half-wave potential of the Nfn/PA/Fe-2 catalyst is 0.879 V, which only decreases by 19 mV after 5000 cycles in alkaline media, exhibiting the excellent

^aDivision of Fuel Cell & Battery, Dalian National Laboratory for Clean Energy, Dalian Institute of Chemical Physics, Chinese Academy of Sciences, Zhongshan Road 457, Dalian 116023, China. E-mail: gqsun@dicp.ac.cn; Tel: +86 411 84379063

^bUniversity of Chinese Academy of Sciences, Beijing 100039, China

† Electronic supplementary information (ESI) available. See DOI: 10.1039/c6ra08654c

electrochemical durability and promising application in fields of metal–air batteries and alkaline fuel cells.

Experimental

Materials

Aniline (C₆H₅NH₂, 99.5%) and ammonium peroxydisulfate ((NH₄)₂S₂O₈, 98%) were purchased from Damao Reagent Corporation (Tianjing, China). Nafion solution (5 wt%) was obtained from DuPont Corporation (Wilmington, USA). Ferric chloride hexahydrate (FeCl₃·6H₂O, 99%) was provided by Sinopharm Chemical Reagent (Shanghai, China). All aqueous solutions were prepared with ultrapure water (18.2 MΩ cm at 25 °C) from a Purelab Flex system (ELGA, England). All chemicals were used directly without further purification except aniline needed to be distilled and flushed with N₂ prior to use.

Synthesis of catalysts

In a typical synthesis, 0.25 mL aniline, 16.10 mg ferric chloride and 10.200 g Nafion solution (5 wt%) were dissolved into 80 mL ultrapure water to form a uniform solution in one ice bath. A freshly prepared ammonium peroxydisulfate solution (31 mg mL⁻¹, 20 mL) was gradually added to the above solution with vigorous stirring. The polymerization reaction was prolonged for 36 h. The excess water was removed by evaporating the reaction system at 90 °C until the solid content was around 10 wt%. The residual water was further totally removed through a 48 h freezing dry process, during which the temperature was fixed at -51 °C and the pressure was maintained at 7–10 Pa. Then, the precursor containing hybrid polymer composite and ferric chloride was obtained. A raw catalyst was acquired by heat-treated the precursor in a N₂ atmosphere at 900 °C for 1 h with an increasing rate of 5 °C min⁻¹ and the weight loss was divided the reduced mass by the total mass. The raw catalyst needed to be pre-leached in 0.5 M H₂SO₄ aqueous solution at 80 °C for 6 h to remove unstable and inactive species and heat treated again in N₂ atmosphere at 900 °C for 3 h. The final catalyst was labelled as Nfn/PA/Fe-2.

For comparison, Nfn/PA-2 was synthesized without ferric chloride during the preparation process. Controlled synthesis was also carried out by varying the mass ratios of Nafion to aniline while the other reaction parameters were constant. The masses of 5 wt% Nafion solution were 0 g, 0.255 g, 2.550 g, 20.400 g and the mass ratios of Nafion to aniline were 0, 0.05 : 1, 0.5 : 1, 4 : 1, respectively. The catalysts were denoted as PA/Fe, Nfn/PA/Fe-0.05, Nfn/PA/Fe-0.5 and Nfn/PA/Fe-4, respectively.

Physical characterization

Transmission electron microscope (TEM, JEM-2011EM, JEOL) equipped with an energy-dispersive spectrometer for elemental mapping was performed on the obtained catalysts. The samples for TEM analysis were prepared by adding a few drops of colloidal suspension onto a hollow copper grid and wicking away the excess liquid with a tissue paper. X-ray diffraction (XRD) patterns of the catalysts were obtained on a D/max-2400X

Ricoh diffractometer with monochromated Cu-Kα radiation (40 kV, 200 mA) at a scan rate of 5° per minute. Thermo-gravimetric analysis (TGA) was carried out using Setsys 16/18 thermoanalytical device (Setaram, France) in N₂ atmosphere (40 mL min⁻¹) with a heating rate 5 °C min⁻¹. X-ray photoelectron spectroscopy (XPS) was carried out on Kratos AMICUS spectrometer (Thermo Scientific) using Al Kα radiation (1486.71 eV). All the binding energies were determined relative to the adventitious C 1s XPS peak at 284.6 eV. XPS PEAK Version 4.1 was used to fit the narrow scan spectra of N 1s after Shirley type background subtraction. Nitrogen absorption-desorption isotherm was measured on a surface area and pore size analyser (NOVA 2200e, Quantachrome Autosorb-iQ). Before analysis, the samples were out-gassed at 300 °C under vacuum for 4 h. The specific surface area was calculated using adsorption data by the Brunauer–Emmett–Teller (BET) method. Pore size distribution curve was computed using the Quenched Solid Density Functional Theory method.

Electrochemical measurements

A CHI 760D potentiostat/galvanostat was used for the electrochemical measurements in a three electrode electrochemical cell installed with a platinum wire as the counter electrode and an Hg/HgO (0.1 M KOH) as the reference electrode. The potentials in this study were normalized to reversible hydrogen electrode (RHE) unless otherwise specified. All electrochemical measurements were carried out at 25 ± 0.5 °C. The sample-coated glassy carbon (GC) electrode was served as the working electrode and the experimental details were described below.

First, a catalyst ink was prepared by mixing the catalyst powder (2.0 mg) with 0.2 mL water, 1.8 mL anhydrous alcohol and 12 μL Nafion solution (5 wt%, DuPont) under mild sonication in a water bath. Next, the catalyst ink (40 μL) was deposited onto the GC surface and the solvent was evaporated at room temperature. The loading for prepared catalyst was fixed at 0.2 mg cm⁻², while the loading of Pt was around 0.02 mg cm⁻² for the commercial Pt/C (20 wt%, JM).

Potential cycling (100 mV s⁻¹) between -0.8 and 0.2 V (vs. Hg/HgO) was applied to each electrode until a stable cyclic voltammetry (CV) curve was obtained in N₂ purged aqueous KOH electrolyte (0.1 M). The activity of electrocatalyst was evaluated by recording the ORR polarization curve in O₂ saturated KOH electrolyte with a positive sweep rate of 10 mV s⁻¹ at 1600 rpm in the rotating disk electrode (RDE) measurements. All the currents in the CV and ORR polarization curves were normalized to the geometric area of the GC electrode. The kinetic current density of the electrocatalyst was determined from the mass-transfer-corrected Tafel plot. Based on ORR polarization curves at different rotating rates, the electron transfer number could be determined by Koutechy–Levich equation:²⁷

$$\frac{1}{j} = \frac{1}{j_k} + \frac{1}{B\omega^{1/2}} \quad (1)$$

$$B = 0.2nFD_{O_2}^{2/3} \nu^{-1/6} c_{O_2} \quad (2)$$

where J is the measured current density. J_k is the kinetic current density. ω is the electrode rotating rate. n is transferred electron number per oxygen molecule. F is the Faraday constant ($F = 96485 \text{ C mol}^{-1}$). D_{O_2} is the diffusion coefficient of O_2 in 0.1 M KOH ($D_{\text{O}_2} = 1.9 \times 10^{-5} \text{ cm}^2 \text{ s}^{-1}$). ν is the kinetic viscosity ($\nu = 0.01 \text{ cm}^2 \text{ s}^{-1}$). c_{O_2} is the bulk concentration of O_2 ($c_{\text{O}_2} = 1.2 \times 10^{-6} \text{ mol cm}^{-3}$). The constant 0.2 is adopted when the rotation speed is expressed in rpm.

During the rotating ring disk electrode (RRDE) measurements, the ring potential was biased at 0.30 V (vs. Hg/HgO). The yield of HO_2^- and the electron transfer number were calculated by the following equations:²⁸

$$\text{HO}_2^- (\%) = 200 \times \frac{I_R/N}{I_R/N + I_D} \quad (3)$$

$$n = \frac{4I_D}{I_D + I_R/N} \quad (4)$$

where N is the collection efficiency ($N = 0.38$), I_D and I_R are the disk current and the ring current, respectively.

The accelerated durability tests (ADTs) of the electrocatalysts were performed in O_2 saturated aqueous KOH electrolyte in the potential range from 0.6 to 1.0 V with a scan rate of 50 mV s^{-1} .

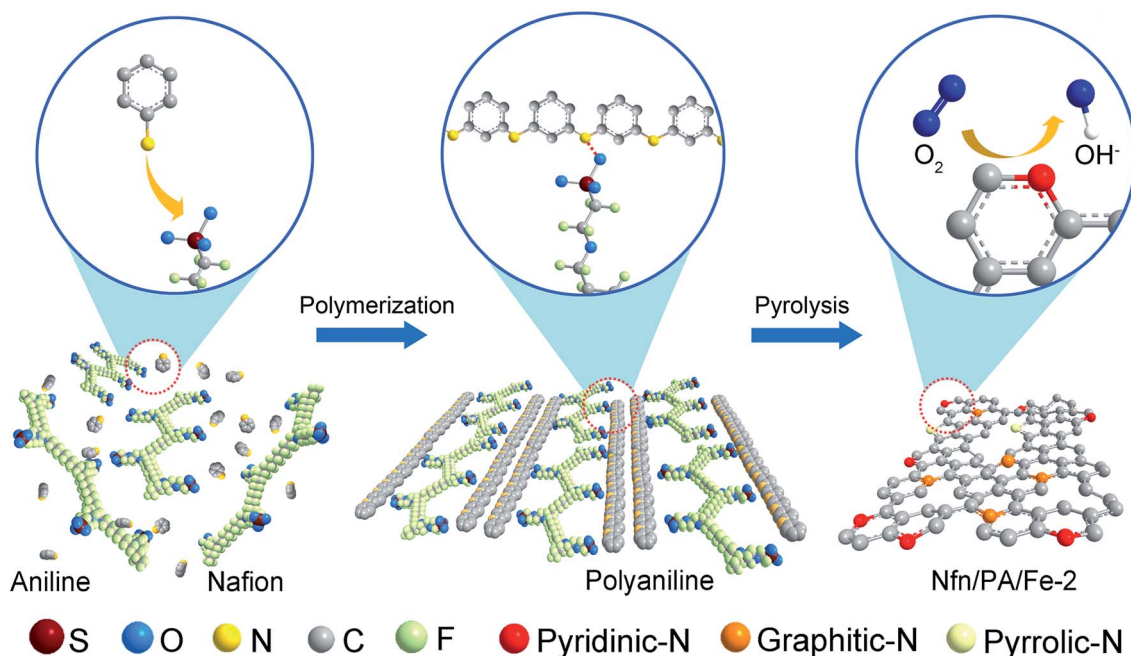
Zn-air battery was tested in a single cell purchased from Shenyang Kejing Auto-instrument Co., Ltd (STC-LI-AIR, Shenyang, China). The loadings of prepared catalysts and Pt/C (60 wt%, JM) on the gas diffusion layer (Teflon-coated carbon fiber paper, 2.54 cm^2) were fixed at 1.0 mg cm^{-2} and $0.1 \text{ mg}_{\text{Pt}} \text{ cm}^{-2}$, respectively. Zn powder and 6 M KOH solution were used as anode and liquid electrolyte, respectively. Measurements were carried out at room temperature *via* a fuel cell test system (Arbin Instrument Corp.) under 80 mL min^{-1} flow rate of O_2 in the cathode.

Results and discussion

Synthesis

On the bases of hybrid polymer matrix composite, the synthesis route of Nfn/PA/Fe-2 is illustrated in Scheme 1. The key step is the *in situ* polymerization of aniline monomers into Nafion framework to form hybrid polymer matrix composite. The relative amount of Nafion to aniline is found to be crucial for the formation of hybrid polymer matrix composite (Scheme S1†). Large amount of Nafion in the reaction system is found to hinder the polymerization of aniline and yellow aniline oligomers are obtained (Fig. S1,† Nfn/PA/Fe-4). The polymerization reaction only takes place when the mass ratio of Nafion to aniline is below 4. The polymer product is green, which is the color of polyaniline (Fig. S1,† PA/Fe, Nfn/PA/Fe-2).

The formation of hybrid polymer matrix composite is approved by the XRD patterns. As shown in Fig. 1a, peak A and B of Nfn/PA-2 is negatively-shifted by 1 and 1.3° with respect to Nafion, respectively, revealing that the polyaniline inserts into the Nafion matrix and enlarges the distance of Nafion chain. In general, the onset decomposition temperature is an indicator of the thermal stability of polymer.^{29,30} The TGA curves of Nfn/PA-2, Nafion, and polyaniline in N_2 atmosphere are compared in Fig. 1b. The onset decomposition temperature of Nfn/PA-2, Nafion and polyaniline is found to be 340, 290 and 230°C , respectively, demonstrating the excellent thermal stability of Nfn/PA-2. The residual weight of Nfn/PA-2, Nafion and polyaniline at 900°C is 23.5, 4.2 and 13.0 wt%, respectively, supporting the increased thermal stability of Nfn/PA-2. Electrostatic interaction in-between the amino groups of polyaniline and the sulfonate groups of Nafion is responsible for the increase of the thermal stability of the hybrid polymer matrix composite,³¹ resulting in the increase of the nitrogen content of prepared catalyst.



Scheme 1 Schematic representation of the synthesis of Nfn/PA/Fe-2.

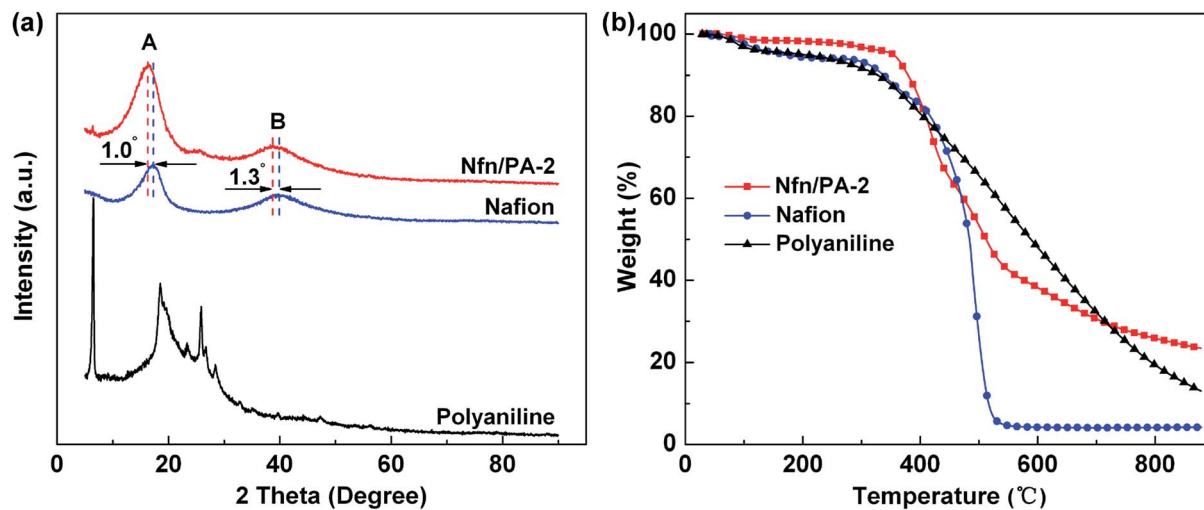


Fig. 1 XRD (a) and TGA curves (b) of Nfn/PA-2 (before pyrolysis), Nafion and polyaniline.

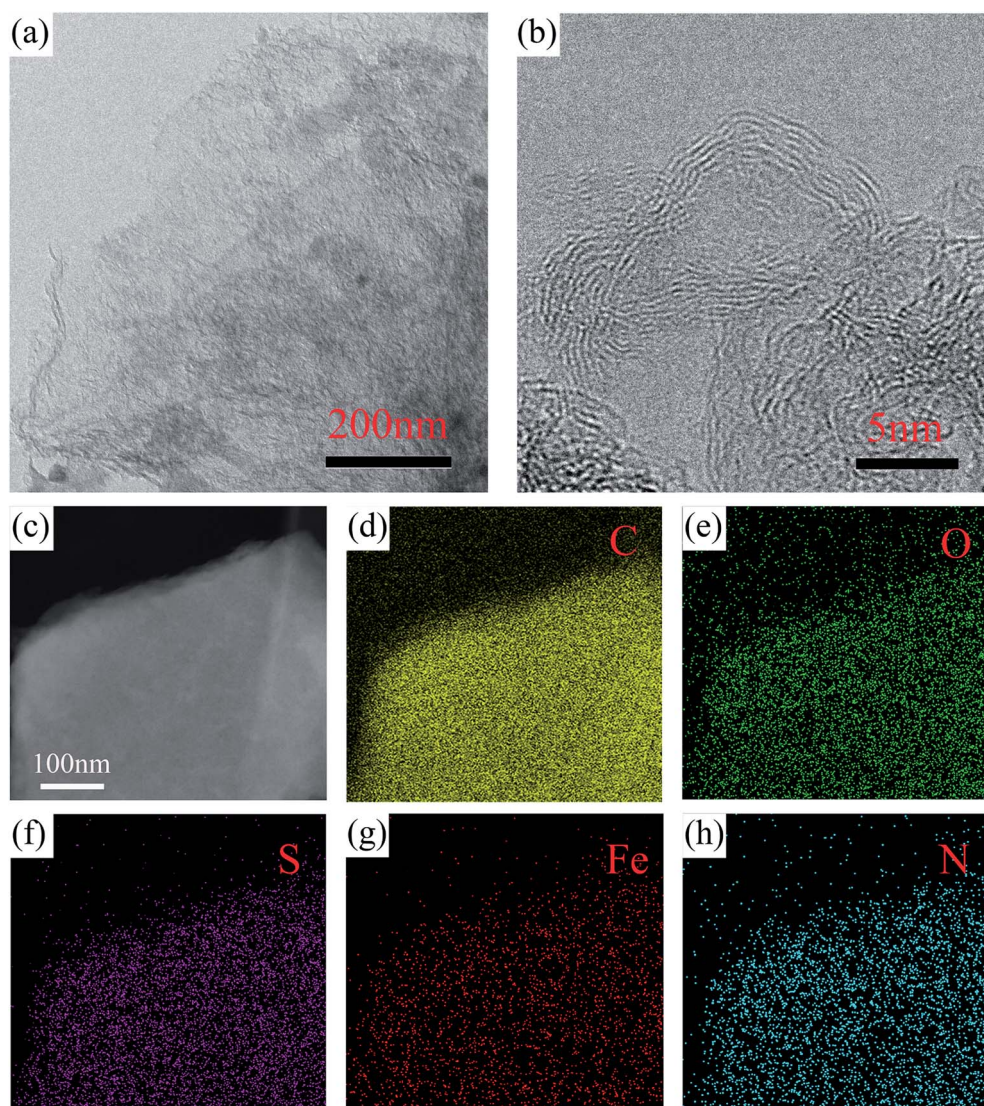


Fig. 2 TEM images at different magnifications (a and b), STEM (c) and element mapping images for carbon (d), oxygen (e), sulfur (f), iron (g) and nitrogen (h) of Nfn/PA/Fe-2.

Physical characterization

The morphologies of the catalysts are shown in Fig. 2 and S2.† Loose structure is observed in the low resolution TEM image of Nfn/PA/Fe-2, which implies the existence of pore structures (Fig. 2a).³² The amorphous carbon structure and the weak lattice fringe image of the Nfn/PA-2 are observed in the high magnification TEM (Fig. S2a†). In contrast, the clear and strong

graphitic fringe image is displayed in PA/Fe (Fig. S2b†). The difference in the graphitic fringe images between Nfn/PA-2 and PA/Fe should be ascribed to the presence of iron element, which is important for the formation of graphitic structure.²¹ The clearest graphitic fringe image is obtained in the Nfn/PA/Fe-2, indicating a further improvement of graphitic structure by the simultaneous existence of iron element and Nafion (Fig. 2b).

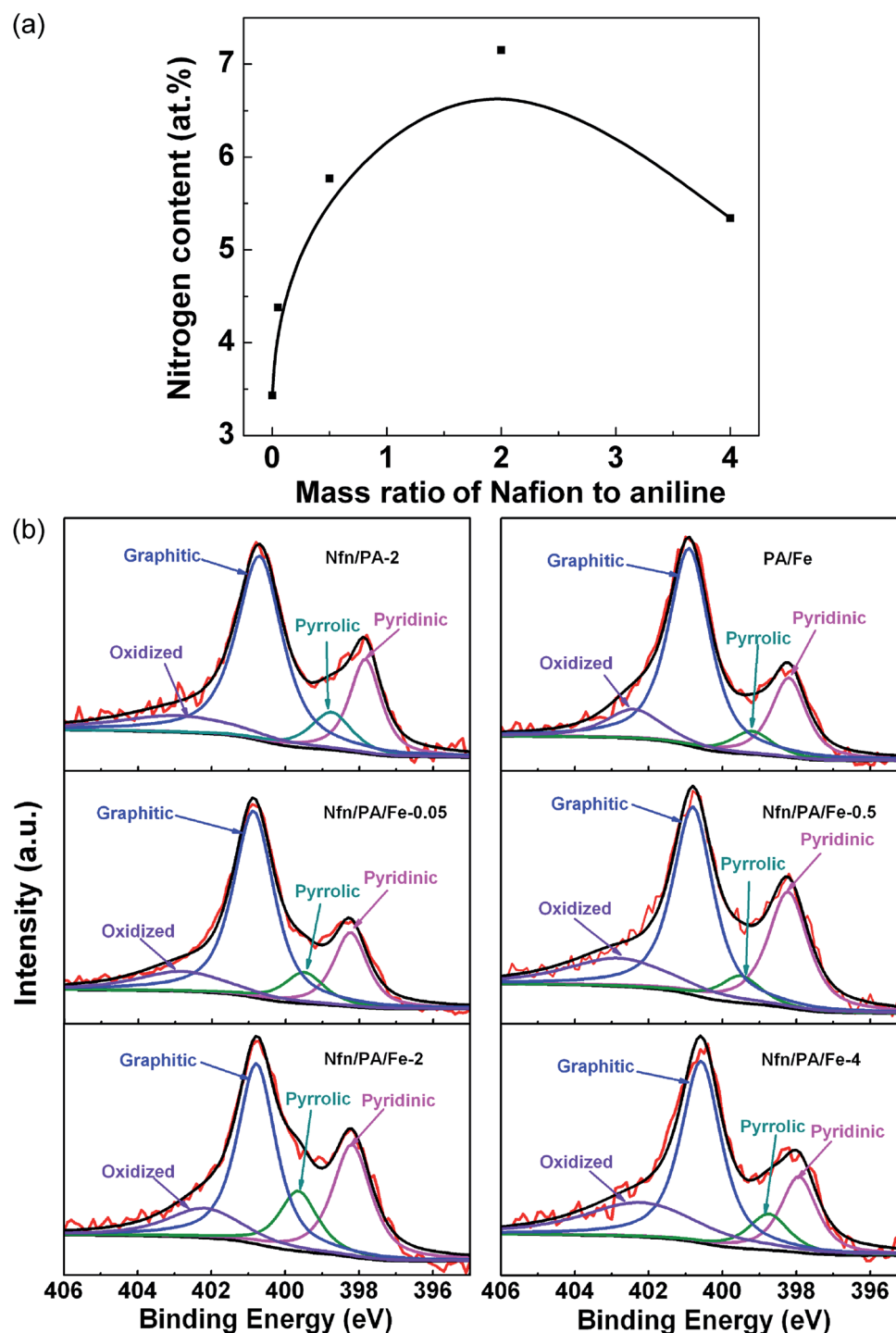


Fig. 3 (a) Curves showing the dependence of the nitrogen contents on the mass ratios of Nafion to aniline (PA/Fe and Nfn/PA/Fe- x , $x = 0.05, 0.5, 2, 4$); (b) N 1s XPS spectra of Nfn/PA-2, PA/Fe, Nfn/PA/Fe-0.05, Nfn/PA/Fe-0.5, Nfn/PA/Fe-2, Nfn/PA/Fe-4.

STEM and associated elemental mapping show the homogeneous distribution of oxygen, iron, sulfur and nitrogen throughout the whole carbon structure for Nfn/PA/Fe-2 (Fig. 2c–h), confirming the success of our synthesis.

XPS spectra of the prepared samples clearly indicate the presence of carbon, nitrogen, oxygen, sulfur, iron in Nfn/PA/Fe-2 (Fig. S3†), which are consistent with the results from elemental mapping in Fig. 2c–h. The presence of sulfur in all the catalysts synthesized here is due to the usage of ammonium peroxydisulfate and Nafion in the synthesis process. The effect of sulfur on ORR activity is still in disputing. Ferrandon *et al.* believe that the sulfur has little effect on ORR activity,³³ while some researchers have reported that sulfur-doped carbon materials show high ORR catalytic activity.^{34–36} The well-resolved C 1s spectra of Nfn/PA/Fe-2 (Fig. S3g†) can be deconvoluted to several single peaks of O–C=O (288.9 eV), C–N and C=O (286.4 eV), C=N and C–O (285.4 eV) and C=C (284.5 eV), indicating the existence of nitrogen-coordinated-carbon structure in the prepared catalyst.³⁷ The iron contents are extremely lower than the nitrogen contents, suggesting that a number of nitrogen functionalities are not coordinated with iron ions at the catalyst surface (Fig. S3b–f†). The iron species may not act as the active sites for ORR, but they have positive contribution to the formation of active sites, which is consistent with the result from B. N. Popov *et al.*³⁸ Fig. S3h† shows the Fe 2p binding energy region for Nfn/PA/Fe-2, which corresponds to two pairs of peaks for Fe³⁺ (711.6 and 724.8 eV) and Fe²⁺ (710.0 and 722.5 eV) with a satellite peak at 716.0 eV. Notably, the signal of typical metallic iron (707.0 eV) is not observed in this work, revealing the absence of metallic iron nanoparticles.³⁹ XRD patterns of the prepared samples are shown in Fig. S4.† Diffraction peaks of iron-containing nanoparticles are not detected in the Nfn/PA/Fe-2. This suggests that the majority of the iron is removed during the acid-leaching step and the trace iron remained is homogeneous distribution in the sample, which is consistent with TEM and XPS results of Nfn/PA/Fe-2 (Fig. 2g and S3h†).

The relationship between the nitrogen contents and the mass ratios of Nafion to aniline is depicted in Fig. 3a. The nitrogen content for PA/Fe and Nfn/PA/Fe-0.05 is 3.43 and 4.38 at%, respectively, remarkable lower than that of Nfn/PA/Fe-2 (7.15 at%) (Table S1†), indicating that an appropriate amount of Nafion can increase the nitrogen content. The nitrogen content of Nfn/PA/Fe-2 is also higher than those of the reported catalysts (Table S2†). However, the aniline is not polymerized if the amount of Nafion is too high. For instance, the nitrogen content of Nfn/PA/Fe-4 is only 5.34 at% when the mass ratio of Nafion to aniline is 4. The N 1s spectra of the samples are shown in Fig. 3b. Four peaks are observed at 398.0 ± 0.2 , 399.2 ± 0.2 , 400.8 ± 0.2 , and 402.4 ± 0.2 eV, which are assigned to pyridinic-N, pyrrolic-N, graphitic-N and oxidized-N, respectively. It can be seen from Table S1† that pyridinic-N and graphitic-N are the dominant species, which are generally considered as efficient ORR active sites.^{39–41}

N₂ adsorption–desorption isotherm curves are measured to evaluate the textural properties of the prepared catalysts and the results are shown in Fig. 4 and Table S1.† The specific surface areas of the samples increases from 545 m² g⁻¹ (PA/Fe) to 1624

m² g⁻¹ (Nfn/PA/Fe-4) with the increase of mass ratio of Nafion to aniline from 0 to 4. The largest specific surface area of Nfn/PA/Fe-4 is consistent with the significant weight loss (85.8%, Table S1†) caused by the decomposition and volatilization of Nafion in the pyrolysis procedure.⁴² Both micropores (<2 nm) and mesopores (2–50 nm) structures are confirmed from pore size distribution curves (Fig. 4b), which afford numerous active sites and enhance the mass transport of O₂.^{23,24}

Electrochemical characterization

The electrocatalytic activities of the catalysts to ORR are examined in 0.1 M KOH solution by CV and RDE measurements. Contrast experiment is also carried out for a state-of-the-art commercial Pt/C catalyst (20% Pt, JM) under the same conditions. In the CV measurements, a typical double-layer capacitance without any obvious redox peaks is observed for all prepared catalysts in N₂-saturated 0.1 M KOH solution (Fig. S5†). The double-layer capacitances of the catalysts increase with the increase of mass ratios of Nafion to aniline, showing the same trend with the specific surface areas (Fig. 4a). As shown by ORR polarization curves in RDE measurements,

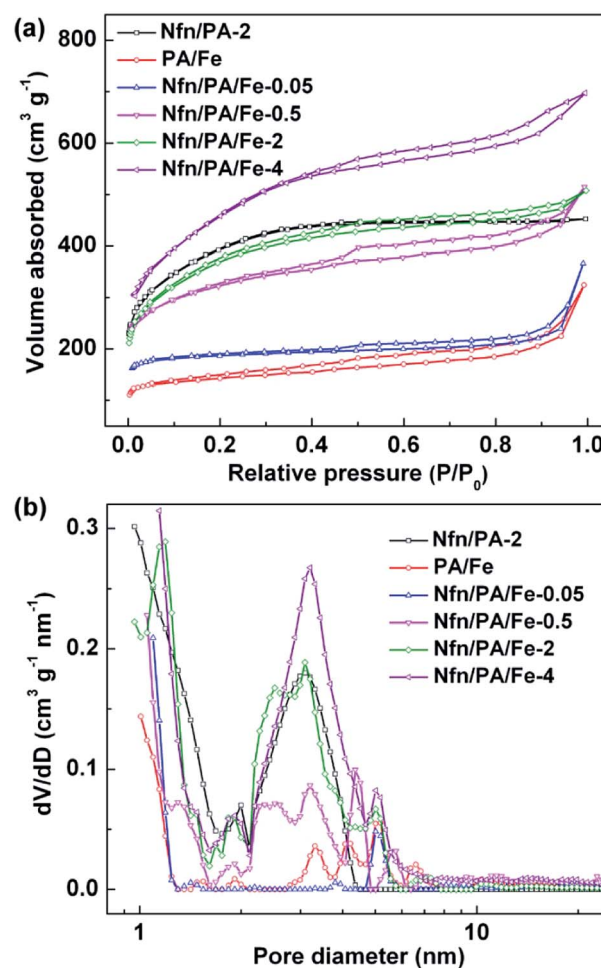


Fig. 4 N₂ adsorption–desorption isotherms (a) and corresponding pore size distribution curves (b) of Nfn/PA-2, PA/Fe, Nfn/PA/Fe-0.05, Nfn/PA/Fe-0.5, Nfn/PA/Fe-2, Nfn/PA/Fe-4.

the half-wave potential of the Nfn/PA-2 and PA/Fe is only 0.757 and 0.720 V, respectively, exhibiting low activity (Fig. 5a). The largest half-wave potential is obtained for the Nfn/PA/Fe-2 (0.879 V), which is higher than that of Pt/C catalyst (0.860 V). Because the loading of Nfn/PA/Fe-2 (0.2 mg cm^{-2}) is higher than that of Pt/C ($0.02 \text{ mg}_{\text{Pt}} \text{ cm}^{-2}$) and the active sites in Nfn/PA/Fe-2 (0.2 mg cm^{-2}) may be more than that in Pt/C ($0.02 \text{ mg}_{\text{Pt}} \text{ cm}^{-2}$). Fig. 5b shows the kinetic current densities before and after normalized by the specific surface areas of the catalysts. While the kinetic current density of Nfn/PA/Fe-2 (9.6 mA cm^{-2}) is 6.9 times of Nfn/PA/Fe-0.05 (1.4 mA cm^{-2}) before the normalization by specific surface area, it decreases to 4.0 times after the normalization, suggesting that the larger specific surface area in Nfn/PA/Fe-2 could be responsible for the enhancement of ORR activity.²⁶

Fig. 5c shows the comparison of the kinetic current densities at 0.85 V of the catalysts with the amounts of accessible nitrogen (nitrogen contents by specific surface areas).⁴³ The same trend is observed for both the kinetic current densities and the amounts of accessible nitrogen. Such finding is not obtained for accessible sulfur and iron (Fig. S6†). Both accessible pyridinic-N and graphitic-N are found to follow the same trend with the kinetic

current density (Fig. 5d), revealing that the real active sites for the ORR would be related to the pyridinic-N and graphitic-N accessible sites.

The yield of HO_2^- and the electron transfer number as the function of the potential are plotted in Fig. S7.† The yields of HO_2^- for Nfn/PA/Fe-2 and Nfn/PA/Fe-4 are below 7.5% and become comparable to that of Pt/C at 0.8 V (Fig. S7a†). The electron transfer numbers of Nfn/PA/Fe-2 and Nfn/PA/Fe-4 are above 3.8 (Fig. S7b†), which are consistent with the results from the Koutechy–Levich plots (Fig. S8†), suggesting a four-electron pathway for ORR.⁸

To assess the electrochemical durability of the catalysts, Nfn/PA/Fe-2 and Pt/C catalysts are cycled between 0.6 V and 1.0 V at 50 mV s^{-1} in 0.1 M KOH under O_2 atmosphere (Fig. 6). After 5000 cycles in alkaline media, the half-wave potential of Nfn/PA/Fe-2 only decreases by 19 mV, which is half of the Pt/C catalyst (37 mV). This suggests the Nfn/PA/Fe-2 holds the excellent electrochemical durability.

The activities of the prepared catalysts are further evaluated the performance in Zn–air cell and a photo of the single cell to test Zn–air battery is shown in Fig. S9.† The peak power density of the cell with Nfn/PA/Fe-2 is 145.7 mW cm^{-2} , which

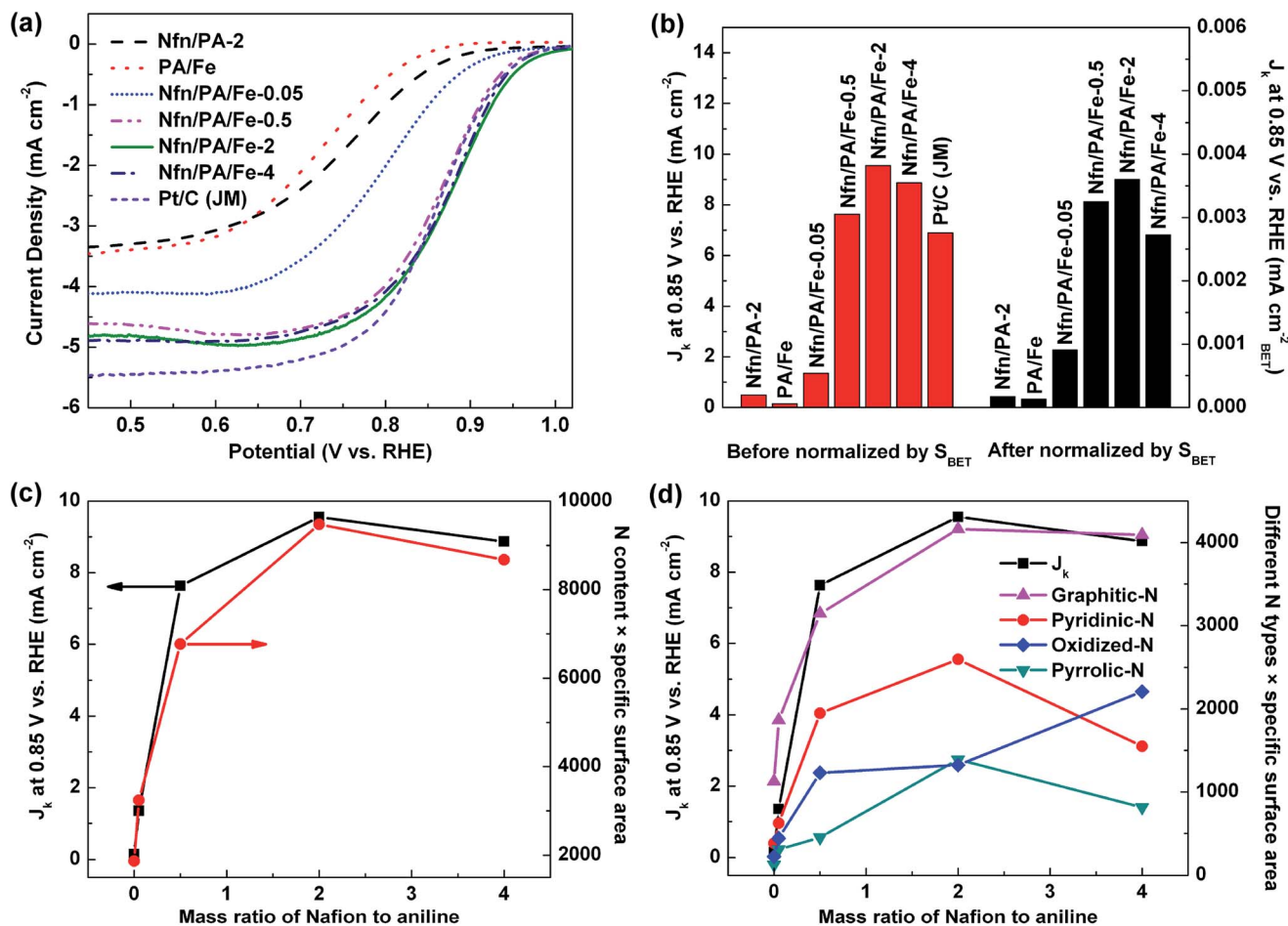


Fig. 5 ORR polarization curves (a) and kinetic current densities at 0.85 V before and after normalized by the specific surface areas (b) of Nfn/PA-2, PA/Fe, Nfn/PA/Fe-0.05, Nfn/PA/Fe-0.5, Nfn/PA/Fe-2, Nfn/PA/Fe-4 and Pt/C (JM); relationship between kinetic current densities of the prepared catalysts and the amounts of accessible nitrogen (c), different nitrogen types (d).

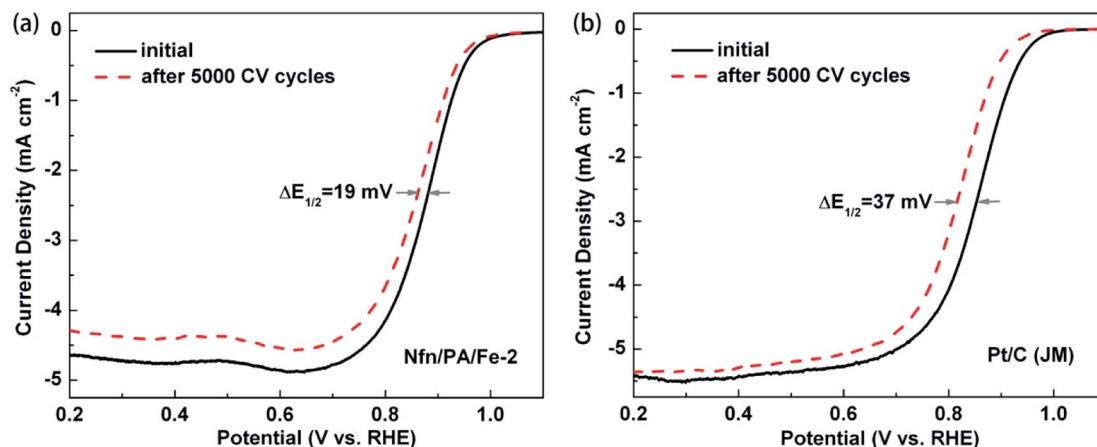


Fig. 6 ORR polarization curves of Nfn/PA/Fe-2 (a) and Pt/C (JM) (b) before and after 5000 CV cycles in O_2 -saturated electrolyte.

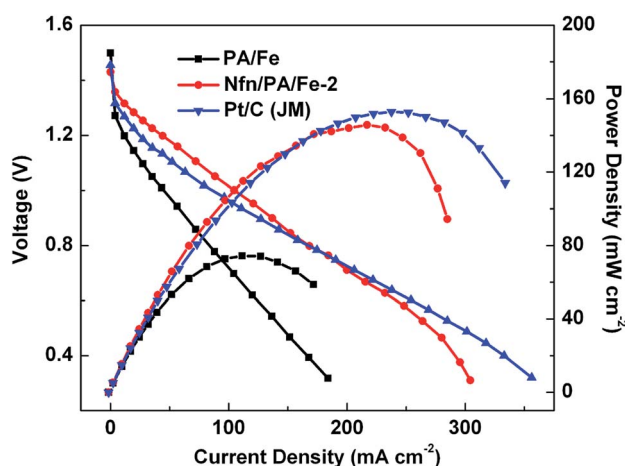


Fig. 7 Polarization and power density curves of Zn-air batteries using PA/Fe, Nfn/PA/Fe-2 and Pt/C (60 wt%, JM) as ORR catalysts.

approaches to the value of commercial Pt/C (152.9 mW cm^{-2}). At the current density lower than 100 mA cm^{-2} , the voltage of the cell with Nfn/PA/Fe-2 is slightly higher than that of Pt/C, and much higher than that of PA/Fe, which supports the best activity of Nfn/PA/Fe-2 as analyzed above. The catalyst layer of cathode with Nfn/PA/Fe-2 (1 mg cm^{-2}) is thicker than that with Pt/C ($0.1 \text{ mg}_{\text{Pt}} \text{ cm}^{-2}$). Note that the mass transport of O_2 is sensitive in the region of higher current density. In general, the cathode is the thinner, the mass transport of O_2 the better.⁴⁴ In this context, the performance of Nfn/PA/Fe-2 is slightly inferior than that of Pt/C in the region of higher current density (Fig. 7).

Conclusions

In situ polymerization of aniline monomers into Nafion framework has been employed to synthesize hybrid polymer matrix composite, which serves as a novel nitrogen precursor for MNC catalyst. The electrostatic interaction between the amino groups of polyaniline and sulfonate groups of Nafion is found to be helpful for the thermal stability of the nitrogen precursor,

which increases the nitrogen content of the catalyst. High specific surface area can be achieved *via* the decomposition and volatilization of Nafion in the pyrolysis procedure. The Nfn/PA/Fe-2 exhibits the best ORR activity, which holds high nitrogen content (7.15 at%) and large specific surface area ($1325 \text{ m}^2 \text{ g}^{-1}$). The half-wave potential of the Nfn/PA/Fe-2 is 0.879 V, which only decreases by 19 mV after 5000 cycles in alkaline media, exhibiting the excellent electrochemical durability. The real active sites of the prepared catalysts would be related to the pyridinic-N and graphitic-N accessible sites. The Zn-air battery with Nfn/PA/Fe-2 as cathode catalyst shows good performance with a peak power density of 145.7 mW cm^{-2} , which is comparable to that with Pt/C catalyst.

Acknowledgements

The authors appreciate the financial supports of the National Basic Research Program of China (2012CB215500) and the National Natural Science Foundation of China Grants (21406222, 21306187).

Notes and references

- 1 M. K. Debe, *Nature*, 2012, **486**, 43–51.
- 2 Z. Chen, D. Higgins, A. Yu, L. Zhang and J. Zhang, *Energy Environ. Sci.*, 2011, **4**, 3167–3192.
- 3 J. Jin, X. Fu, Q. Liu and J. Zhang, *J. Mater. Chem. A*, 2013, **1**, 10538–10545.
- 4 Y. Nie, X. Xie, S. Chen, W. Ding, X. Qi, Y. Wang, J. Wang, W. Li, Z. Wei and M. Shao, *Electrochim. Acta*, 2016, **187**, 153–160.
- 5 X. Fu, Y. Liu, X. Cao, J. Jin, Q. Liu and J. Zhang, *Appl. Catal., B*, 2013, **130**, 143–151.
- 6 H. T. Chung, J. H. Won and P. Zelenay, *Nat. Commun.*, 2013, **4**, 1922.
- 7 J. Y. Cheon, T. Kim, Y. Choi, H. Y. Jeong, M. G. Kim, Y. J. Sa, J. Kim, Z. Lee, T.-H. Yang, K. Kwon, O. Terasaki, G.-G. Park, R. R. Adzic and S. H. Joo, *Sci. Rep.*, 2013, **3**, 2715.

- 8 F. Liu, L. Liu, X. Li, J. Zeng, L. Du and S. Liao, *RSC Adv.*, 2016, **6**, 27535–27541.
- 9 H. A. Gasteiger and N. M. Marković, *Science*, 2009, **324**, 48–49.
- 10 Y. Nie, L. Li and Z. Wei, *Chem. Soc. Rev.*, 2015, **44**, 2168–2201.
- 11 H. R. Byon, J. Suntivich and Y. Shao-Horn, *Chem. Mater.*, 2011, **23**, 3421–3428.
- 12 G. Wu, K. L. More, P. Xu, H.-L. Wang, M. Ferrandon, A. J. Kropf, D. J. Myers, S. Ma, C. M. Johnston and P. Zelenay, *Chem. Commun.*, 2013, **49**, 3291–3293.
- 13 U. I. Kramm, M. Lefevre, N. Larouche, D. Schmeisser and J.-P. Dodelet, *J. Am. Chem. Soc.*, 2014, **136**, 978–985.
- 14 K. Gong, F. Du, Z. Xia, M. Durstock and L. Dai, *Science*, 2009, **323**, 760–764.
- 15 K. Strickland, E. Miner, Q. Jia, U. Tylus, N. Ramaswamy, W. Liang, M. T. Sougrati, F. Jaouen and S. Mukerjee, *Nat. Commun.*, 2015, **6**, 7343.
- 16 J. Koh, S. H. Park, M. W. Chung, S. Y. Lee and S. I. Woo, *RSC Adv.*, 2016, **6**, 27528–27534.
- 17 R. Kothandaraman, V. Nallathambi, K. Artyushkova and S. C. Barton, *Appl. Catal., B*, 2009, **92**, 209–216.
- 18 M. K. Rybarczyk, M. Lieder and M. Jablonska, *RSC Adv.*, 2015, **5**, 44969–44977.
- 19 Q. Wang, Z. Y. Zhou, Y. J. Lai, Y. You, J. G. Liu, X. L. Wu, E. Terefe, C. Chen, L. Song, M. Rauf, N. Tian and S. G. Sun, *J. Am. Chem. Soc.*, 2014, **136**, 10882–10885.
- 20 C. Gumeci, N. Leonard, Y. C. Liu, S. McKinney, B. Halevi and S. C. Barton, *J. Mater. Chem. A*, 2015, **3**, 21494–21500.
- 21 W. Ding, L. Li, K. Xiong, Y. Wang, W. Li, Y. Nie, S. Chen, X. Qi and Z. Wei, *J. Am. Chem. Soc.*, 2015, **137**, 5414–5420.
- 22 J. Xu, Q. Yu and L. Guan, *J. Mater. Chem. A*, 2015, **3**, 7093–7099.
- 23 F. Jaouen, M. Lefèvre, J.-P. Dodelet and M. Cai, *J. Phys. Chem. B*, 2006, **110**, 5553–5558.
- 24 H.-W. Liang, W. Wei, Z.-S. Wu, X. Feng and K. Müllen, *J. Am. Chem. Soc.*, 2013, **135**, 16002–16005.
- 25 J. Wei, Y. Liang, X. Zhang, G. P. Simon, D. Zhao, J. Zhang, S. Jiang and H. Wang, *Nanoscale*, 2015, **7**, 6247–6254.
- 26 H. W. Liang, X. Zhuang, S. Bruller, X. Feng and K. Mullen, *Nat. Commun.*, 2014, **5**, 4973.
- 27 H. Yin, C. Zhang, F. Liu and Y. Hou, *Adv. Funct. Mater.*, 2014, **24**, 2930–2937.
- 28 Y. Liu, B. Zhao, Y. Zhang, H. Zhang, K. Zhan, J. Yang and J. Li, *RSC Adv.*, 2016, **6**, 32676–32684.
- 29 K. W. Chan, C. Z. Liao, H. M. Wong, K. W. Kwok Yeung and S. C. Tjong, *RSC Adv.*, 2016, **6**, 19417–19429.
- 30 T. Y. Zhou, G. C. P. Tsui, J. Z. Liang, S. Y. Zou, C. Y. Tang and V. Mišković-Stanković, *Composites, Part B*, 2016, **90**, 107–114.
- 31 X. Wang and Q. Zhang, *Polym. Int.*, 2004, **53**, 698–707.
- 32 Y. Wang and X. Jiang, *ACS Appl. Mater. Interfaces*, 2013, **5**, 11597–11602.
- 33 M. Ferrandon, A. J. Kropf, D. J. Myers, K. Artyushkova, U. Kramm, P. Bogdanoff, G. Wu, C. M. Johnston and P. Zelenay, *J. Phys. Chem. C*, 2012, **116**, 16001–16013.
- 34 Z. Yang, Z. Yao, G. Li, G. Fang, H. Nie, Z. Liu, X. Zhou, X. Chen and S. Huang, *ACS Nano*, 2012, **6**, 205–211.
- 35 J. Liang, Y. Jiao, M. Jaroniec and S. Z. Qiao, *Angew. Chem., Int. Ed.*, 2012, **51**, 11496–11500.
- 36 X. Wang, J. Wang, D. Wang, S. Dou, Z. Ma, J. Wu, L. Tao, A. Shen, C. Ouyang, Q. Liu and S. Wang, *Chem. Commun.*, 2014, **50**, 4839.
- 37 Z. Lin, G. Waller, Y. Liu, M. Liu and C.-P. Wong, *Adv. Energy Mater.*, 2012, **2**, 884–888.
- 38 V. Nallathambi, J.-W. Lee, S. P. Kumaraguru, G. Wu and B. N. Popov, *J. Power Sources*, 2008, **183**, 34–42.
- 39 H. Jiang, Y. Yao, Y. Zhu, Y. Liu, Y. Su, X. Yang and C. Li, *ACS Appl. Mater. Interfaces*, 2015, **7**, 21511–21520.
- 40 L. Lai, J. R. Potts, D. Zhan, L. Wang, C. K. Poh, C. Tang, H. Gong, Z. Shen, J. Lin and R. S. Ruoff, *Energy Environ. Sci.*, 2012, **5**, 7936–7942.
- 41 G. Panomsuwan, N. Saito and T. Ishizaki, *Phys. Chem. Chem. Phys.*, 2015, **17**, 6227–6232.
- 42 J. Zhang, Z. Zhao, Z. Xia and L. Dai, *Nat. Nanotechnol.*, 2015, **10**, 444–452.
- 43 C. Dominguez, F. J. Perez-Alonso, M. A. Salam, S. A. Al-Thabaiti, M. A. Pena, L. Barrio and S. Rojas, *J. Mater. Chem. A*, 2015, **3**, 24487–24494.
- 44 S. Lee, M. Choun, Y. Ye, J. Lee, Y. Mun, E. Kang, J. Hwang, Y.-H. Lee, C.-H. Shin, S.-H. Moon, S.-K. Kim, E. Lee and J. Lee, *Angew. Chem., Int. Ed.*, 2015, **32**, 9320–9324.